Check for updates

Manipulating the morphology of the nano oxide domain in AuCu–iron oxide dumbbell-like nanocomposites as a tool to modify magnetic properties†

Sharif Najafishirtari, [iD] [a] Aidin Lak,[b] Clara Guglieri,[c] Sergio Marras,[d] Rosaria Brescia,[e] Sergio Fiorito,[bf] Elaheh Sadrollahi,[g] Fred Jochen Litterst,[g] Teresa Pellegrino, [iD] [b] Liberato Manna[a] and Massimo Colombo*[a]

We report the colloidal synthesis of hybrid dumbbell-like nanocrystals (NCs) which feature a plasmonic metal domain (M) attached to a morphologically-tunable magnetic oxide domain (MOx). We highlight how the modulation of the amount of oleic acid (OlAc) in the synthesis mixture influences the final composition of the M domain, the morphology of the MOx domain and, consequently, the magnetic properties of the hetero-structures. In the presence of high amounts of OlAc, a crystalline, magnetite MOx is mainly formed, coupled with a partial dealloying between Au and Cu in the M domain. Decreasing the amount of OlAc preserved the AuCu alloy and resulted in the formation of core–shell structures in the MOx. Here, a disordered, poorly crystalline, glass-like maghemite shell was coupled with a highly disordered iron rich core. An investigation into the magnetic properties revealed that the disordered phase was likely responsible for the observed exchange bias, rather than the interfacial stress between the M and MOx.

1. Introduction

Hybrid magnetic nanocomposites have attracted the attention of many researchers with regards to their potential use in various technological applications, ranging from biomedical ones to electronic, waste water treatment and catalysis ones, due to their intriguing multifunctional properties.[1–7] Single-phase nanomaterials can be combined in different morphological arrangements, forming multi-phase nanocomposites in order to successfully combine the functionalities of each individual phase. Furthermore, synergetic properties, which are either not present in the single phases or not significant, can be obtained. For example, electronic or mechanical properties can be improved using a core/shell morphology.[8,9] In the case of magnetic nanocomposites, the core/shell morphology has shown potential technological value in a wide range of applications[10] such as recording media[11] and spintronic devices[12,13] with respect to an exchange coupling at the core/shell interface which emanate from the different magnetic properties of the core and the shell, typically observed as an exchange bias.[14] More specifically, Fe/Fe oxide core/shell nanoparticles (NPs) are also considered valuable in biomedical applications such as magnetic hyperthermia, magnetic resonance imaging, and drug delivery.[15–19] The main reason for this lies in the synergy that is provided by the high magnetization of the core along with the stability and the biocompatibility of the shell,[15] as the Fe oxide shell behaves like a protecting layer which prevents the Fe cores from oxidation.[1] A metal oxide domain (MOx) can be also epitaxially grown on a metal NP (M), forming a dumbbell morphology to achieve interesting interfacial properties. The high anisotropic magnetic properties of such materials make them valuable in biological applications,[20–22] while the presence of a specific metal may provide additional catalytic[23–25] and plasmonic features,[26,27] or dual surface functionalization properties exploitable for targeting and drug delivery or dual pH and thermo-responsive coatings.[28,29] For instance, Peng et al. have

[a]Nanochemistry Department, Istituto Italiano di Tecnologia, Via Morego 30, 16163 Genoa, Italy. E-mail: massimo.colombo@iit.it

[b]Nanomaterials for Biomedical Applications, Istituto Italiano di Tecnologia, Via Morego 30, 16163 Genoa, Italy

[c]Elettra Sincrotrone, 34149 Basovizza, Trieste, Italy

[d]Materials Characterization Facility, Istituto Italiano di Tecnologia, Via Morego 30, 16163 Genoa, Italy

[e]Electron Microscopy Facility, Istituto Italiano di Tecnologia, Via Morego 30, 16163 Genoa, Italy

[f]Università degli Studi di Genova, Via Dodecaneso, 31, 16146, Genoa, Italy

[g]Institut für Physik der Kondensierten Materie, Technische Universität Braunschweig, 38106 Braunschweig, Germany
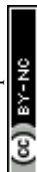
reported the synthesis of bifunctional Ag/Fe oxide hybrid nanomaterials, specifically dumbbells, using Fe/Fe oxide core/shell NPs as seeds for the further growth of the Ag.[26] They have investigated the effects of different synthetic conditions on the size and number of Ag domains as well as on the morphology of the oxide domain. Similar NPs have also been synthesized by Mao *et al.*[30] Chandra *et al.* studied the Au/Fe oxide nanocomposites and reported a tunable exchange bias for magnetic properties through manipulating the sizes of two domains.[20] Other similar heterostructures have shown promising features for use as dual magnetic and optic probes for cell imaging applications[31] or have been successfully used for the sensitive and selective turn-on fluorescent detection of cyanide.[32] The use of bifunctional catalytic-magnetic heterostructures in liquid phase reactions is also reported. Using such nanocomposites, the catalysts can be simply separated and recovered with an external magnet.[33]

With regard to the wide variety of potential applications of the aforementioned hybrid nanocomposites, it is important to explore the synthesis of new materials that have these characteristics. In this work, we report a procedure for the synthesis of colloidal dumbbell-like nanocrystals (NCs) that feature a plasmonic metal domain (*i.e.* AuCu bimetallic phase) and a magnetic metal oxide domain that is characterized by a core/shell morphology. In this regard, we established the relationship between the conditions of the synthesis and both (i) the final composition of the AuCu domain and (ii) the morphology of the oxide domain. In the presence of a low amount of OlAc, the AuCu domain was preserved from partial dealloying, and the MOx domains mainly developed a core/shell morphology. The core was made of a highly disordered Fe-rich phase, and the shell was constituted by a poorly crystalline, glass-like maghemite phase. The presence of a highly disordered glass-like phase undesirably suppressed the magnetic properties of the NCs. Increasing the amount of OlAc in the synthesis mixture caused a partial dealloy in the AuCu domains and resulted in the subsequent formation of heterostructures with a crystalline magnetite MOx domain, leading to enhanced magnetic properties. The results of our work provide insight into the synthesis of complex nanocomposites and their intrinsic properties, and they are potentially of value *e.g.* to biomedical applications due to their combined plasmonic and magnetic properties.

2. Experimental

2.1. Chemicals

Oleylamine (OlAm, 70%), $HAuCl_4 \cdot 3H_2O$, 1-octadecene (ODE, technical grade 90%), oleic acid (OlAc, technical grade 90%), iron pentacarbonyl (>99.99% trace metals basis), solvents (ethanol, isopropanol, toluene and *n*-hexane) were purchased from Sigma-Aldrich while $CuCl_2$ dihydrate (99+%) was purchased from Alfa Aesar and γ-Al_2O_3 from Strem Chemicals. All chemicals were used as received without further purifications.

2.2. Synthesis of AuCu–iron oxide (AuCu@FeOx) NCs

AuCu@FeOx NCs were synthesized using a seed-mediated growth method,[24] starting from pre-made AuCu NCs as
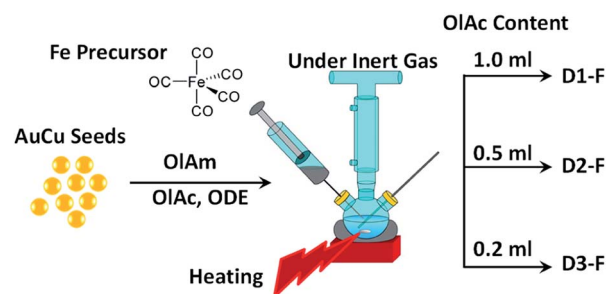
Scheme 1 Schematic illustration of the synthesis procedure. Indeed, all conditions were similar except for the content of OlAc in the reaction mixture.

described elsewhere.[34] In order to induce different oxidation of Fe, a different volume of OlAc was used in the syntheses *i.e.* 1.0, 0.5 and 0.2 ml while the rest of the conditions were kept similar to those that we have previously reported.[24] The samples were tagged as D1-F, D2-F and D3-F, corresponding to the NCs synthesized using 1.0, 0.5 and 0.2 ml of OlAc, respectively. The simplified synthesis procedure is schematically illustrated in Scheme 1, highlighting the difference in the synthetic conditions.

2.3. Characterization

2.3.1. Transmission electron microscopy (TEM). Overview bright-field (BF) TEM images were acquired with a JEOL JEM-1011 instrument equipped with a thermionic W source operating at 100 kV. Energy-filtered TEM (EFTEM) and high-resolution TEM (HRTEM) images were obtained using an image-C_s-corrected JEOL JEM-2200FS TEM with a Schottky emitter, equipped with an in-column image filter (Ω-type) and operating at 200 kV. The elemental maps were obtained by using the three-windows method at the O K, Fe K and Cu L_{23} core-loss edges. Overview high-angle annular dark field- scanning TEM (HAADF-STEM) images were acquired on a FEI Tecnai G2 F20 TWIN TMP TEM.

2.3.2. Elemental analysis. The chemical composition of the NCs was measured by Inductively Coupled Plasma-Optical Emission Spectroscopy (ICP-OES) using an iCAP 6000 Thermo Scientific spectrometer. A specific volume of the colloidal solution was digested in HCl/HNO_3 3 : 1 (v/v) overnight, diluted with deionized water (14 μS) and filtered using a PTFE filter before the measurement.

2.3.3. Optical absorption spectroscopy. The measurements were performed using a Varian Cary 5000 UV-visible-NIR spectrophotometer in a single path configuration in the range of 200–800 nm at a scanning rate of 10 nm s^{-1}. Initially, the background signal was collected from the solvent in a 1.5 ml cuvette. Then, a specific volume of the colloidal solution was added and mixed to get a homogenous mixture from which the spectrum was collected. The spectra were finally normalized to have an intensity between 0–1 in order to get a better comparison.

2.3.4. X-ray diffraction (XRD). XRD patterns were recorded on a Rigaku SmartLab X-ray diffractometer equipped with a 9

kW Cu Kα rotating anode (operating at 40 kV and 150 mA) and a D\teX Ultra 1D detector set in X-ray reduction mode. Samples were prepared by drop casting the solution on a zero-diffraction silicon wafer. The diffraction patterns were collected at room temperature in a Bragg–Brentano geometry over an angular range: $2\theta = 20–85°$, with a step size of $0.02°$ and a scan speed of $0.2°$ min^{-1}. XRD data analysis was carried out using PDXL 2.7.2.0 software from Rigaku.

2.3.5. X-ray absorption fine structure spectroscopy (XAFS). Measurements were performed at the XAFS beamline at the Elettra synchrotron light source[35] in Trieste, Italy. The NCs were initially deposited on alumina, then diluted with a polyvinylpyrrolidone (PVP) powder and pressed into pellets. The pellets were mounted onto a special motorized sample holder so that the desired sample could be exposed to the beam without opening the sample chamber. The X-ray absorption near edge structure (XANES) and the extended X-ray absorption fine structure (EXAFS) spectra were collected at the Fe K-edge (7112 eV), Cu K-edge (8979 eV) and Au L_3-edge (11 919 eV) in transmission mode using ion chambers detectors. The spectra of the references Fe_3O_4 (magnetite), γ-Fe_2O_3 (maghemite), α-Fe_2O_3 (hematite), Fe foil, Cu and Au foils were collected for comparison and/or signal calibration. The analysis was performed according to standard procedures.[36] The data were

normalized after background subtraction using the Athena code within the Demeter package (version 0.9.25).[37] The EXAFS signals were extracted from the spectra by using the Athena software, removing the background by a cubic spline polynomial fitting and normalizing the magnitude of the oscillations to the edge jump. The corresponding pseudoradial distribution function around the photoabsorbing atom was obtained by performing the Fourier transform, FT. The data fitting was then accomplished in both the R space and q-space, considering the selected models using the Artemis code within the same Demeter package.

2.3.6. Mössbauer spectroscopy. ^{57}Fe absorption Mössbauer spectroscopy was performed on materials from D1-F and D3-F in a standard spectrometer. We used about 25 mCi of a gamma radiation source of ^{57}Co in a rhodium matrix which was kept at room temperature. The absorbers had a few mg of material yielding less than 0.1 mg cm^{-2} ^{57}Fe. Absorber temperatures could be varied using a He-flow cryostat (CRY-OVAC). Data analysis was performed using MOSSWINN software.[38]

2.3.7. Magnetic measurement. Field and temperature dependent magnetic measurements were carried out using a Magnetic Property Measurement System (Quantum Design MPMS-XL EverCool) on immobile particles. The immobile
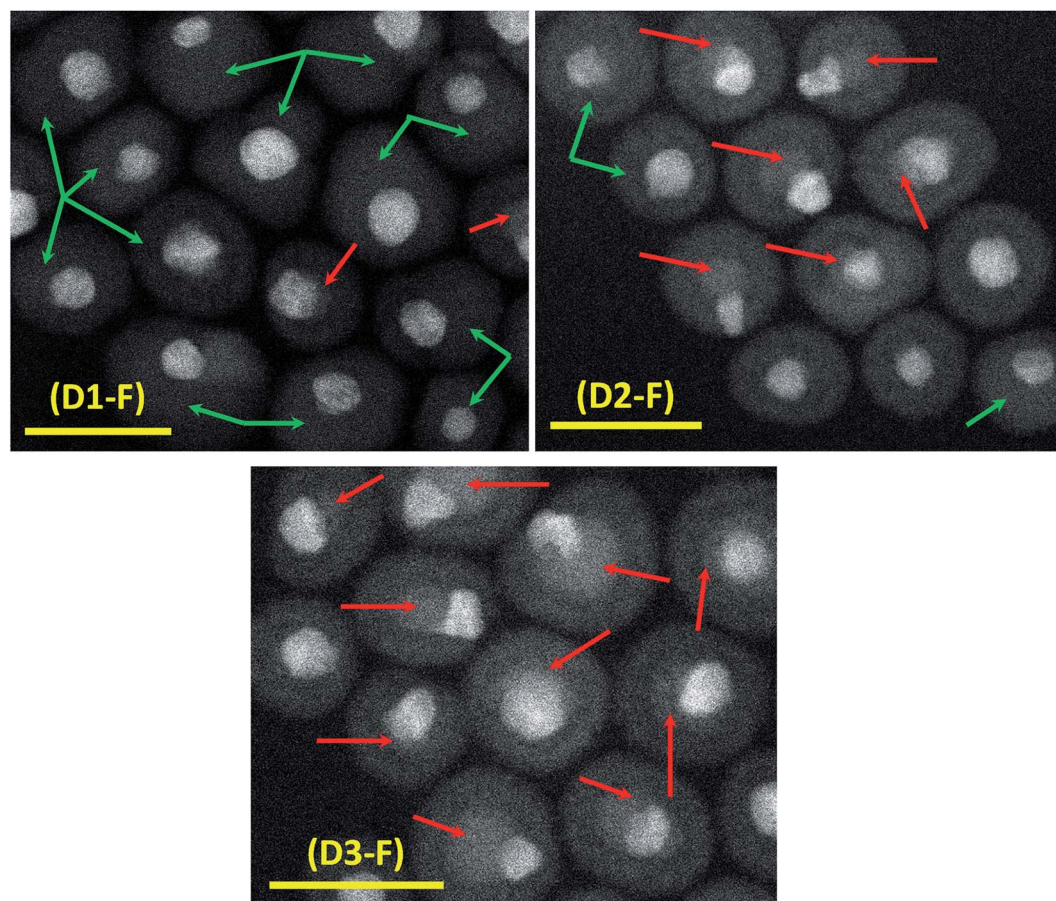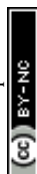

Fig. 1 HAADF-STEM image of the as-prepared AuCu@FeOx colloidal NCs; scale bars = 20 nm. Some of the NCs which had a core/shell morphology in the MOx domains are marked with red arrows, while the homogeneous oxide domains are highlighted by the green arrows.

samples were prepared by mixing 100 μL of a particle solution at an iron concentration of approx. 0.5 g_{Fe} L^{-1} with 60 mg gypsum in a designated polycarbonate capsule and letting it thoroughly solidify. Zero-field-cooled (ZFC) and field-cooled (FC) magnetization measurements *vs.* temperature were performed on identical samples in 5 mT cooling fields. The magnetization curves were corrected with respect to the diamagnetic contributions of Au, Cu, water, and gypsum using the automatic background subtraction routine. The curves were normalized to the iron concentration, as obtained from the elemental analysis.

3. Results and discussion

3.1. Structural properties

The successful synthesis of dumbbell-like AuCu–Fe_3O_4 NCs had already been reported by our group.[24] In the present work, we further explored the role of a specific surfactant, namely OlAc, and the impact it has on the final properties of the NCs. It has been shown that the surfactant ratio can control the morphology of the NCs.[39] No other surfactants or polymers (*e.g.* polyvinylpyrrolidone,[40] ethanolamine[41]) have been investigated in this study, as the simple modification of the OlAc volume was sufficient to trigger the properties of the NCs in the desired direction. Three different volumes of OlAc were used in the synthesis protocol in order to manipulate the properties of the heterostructures. A similar approach has been reported for the synthesis of Fe NPs.[42] The three different volumes of OlAc resulted in three samples that were characterized by a different population of dumbbell-like NCs having a MOx domain with a core/shell morphology. The HAADF-STEM images of the synthesized NCs are shown in Fig. 1. Examples of NCs that had

a MOx domain with a core/shell morphology are marked with red arrows. Examples of NCs in which the MOx domains were characterized by a uniform composition are instead highlighted with green arrows (see Fig. S1† for lower-magnification images along with the size distributions of both the M and MOx domains). The mean size of the M domain and the diameter of MOx domain were obtained by statistical analysis on the TEM images, and they were ~5.7 and ~15.7 nm, respectively (see Table 1 for details). It is noteworthy that the size of M domains was close to the value that was obtained from the initial AuCu seeds (see Fig. S2†), as has already been reported elsewhere.[24] By means of EDS, we have previously shown that the Au and Cu would stay localized in the M domain while the Fe and O were detected within the boundary of the MOx.[24] Additionally, the EFTEM analysis here also revealed a higher density of Fe coupled with a lower density of O in the core region of the core/shell MOx domains (see Fig. 2). By HRTEM, we found out that the MOx shell of these NCs was most frequently composed of few nanometer-sized crystalline domains, most of them matching a cubic spinel structure of magnetite/maghemite, two phases not distinguishable by HRTEM (see Fig. S3†). While an EFTEM map is not shown for Au in Fig. 2, due to the high energy of the optimum core-loss edge for elemental map acquisition (M45 edge at 2206 eV), the Cu was localized in the M domain. The elemental composition of the samples was also analyzed by ICP-OES, and it revealed that the Au : Cu ratio was the same as the initial seeds, as is summarized in Table 1. In addition, the (Au + Cu)/Fe ratio was similar among the samples.

The plasmonic response of the AuCu domains in the NCs was investigated by UV-visible light spectroscopy, and it was compared with that of the AuCu seeds (see Fig. S4†). While no significant difference could be observed among the nano-dumbbells, a shift was observed for the plasmon peak of the AuCu, which is indicative of a change in the local dielectric environment as a result of its attachment to iron oxide.[24]

The structural properties of the NCs were analyzed by XRD and the results are shown in Fig. 3. The XRD patterns of all three samples were representative of two major phases, *i.e.* tetra-auricupride (a tetragonal AuCu phase) and an inverse spinel iron oxide phase, which matched with magnetite (see discussion below for further details on this assignment). From the normalization of the XRD patterns based on the most intense diffraction peak ($2\theta = 40.466$, ICSD: 42574), it is evident that the intensity of the peaks associated to the spinel phase decreased from D1-F to D3-F (*i.e.* by a decrease in the amount of OlAc). As the samples contained the same (Au + Cu)/Fe ratio (see Table 1), and since no other Fe-containing crystalline phases could be
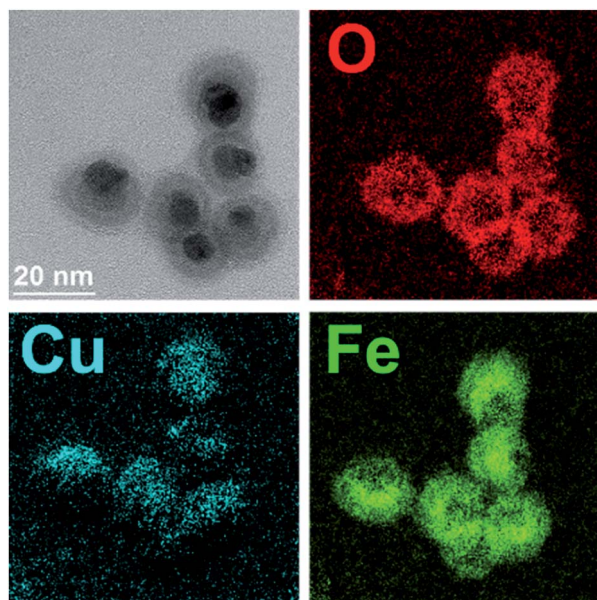

Fig. 2 Zero-loss filtered BF–TEM image and corresponding elemental maps for Cu Cyan), Fe (green) and O (red), showing an Fe-rich core in the metal oxide domain. The data was collected from D3-F sample.

Table 1 Summary of NCs' properties from statistical and elemental analyses

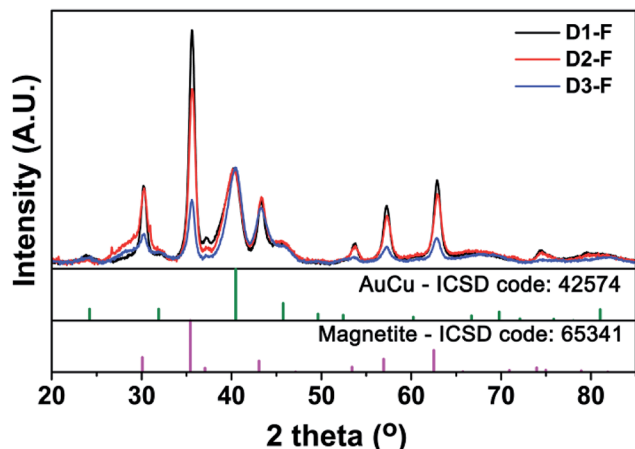| Sample tag	D1-F	D2-F	D3-F
M mean size	5.7 ± 1.4 nm	5.5 ± 0.8 nm	5.7 ± 1.2 nm
MOx mean size	15.2 ± 2.4 nm	16.4 ± 5.4 nm	15.5 ± 3.6 nm
Au : Cu (molar)	54.3 : 45.7	53.5 : 46.5	54.3 : 45.7
(Au + Cu)/Fe (molar)	0.14	0.14	0.13

Fig. 3 X-ray diffraction (XRD) pattern of the as-synthesized AuCu@-FeOx dumbbell NCs. Experimental data are compared with the Inorganic Crystal Structure Database (ICSD) patterns.

detected, the decrease in the signal intensity has to be related to an increase in the amorphous nature of the sample. It is noteworthy that such an increase in the amorphous nature correlates with the increase in the population of NCs with a core/shell morphology in the MOx domains. From the analysis of the XRD patterns, it is also possible to observe that the position of the AuCu main peak (around $2\theta = 40°$) slightly shifted to lower 2θ

(less than 1°), from D3-F to D1-F. This behavior could be indicative of a partial, but minor, dealloying between Au and Cu,[43] probably due to the oxidizing nature of the OlAc.

Further insights into the local structural properties of the NCs were provided by XAFS. The spectra were collected at different absorption edges, namely at the Au L_3-edge (11 919 eV), Cu K-edge (8979 eV) and Fe K-edge (7112 eV). The XANES spectra of the NCs at different edges are presented in Fig. S5.† It is evident from the data at the Au L_3-edge (Fig. S5a†) that the samples had quite similar absorptions spectra that resemble the XANES spectrum of a AuCu alloy,[24] and there was no shift in the absorption edge among the samples. Interestingly, with respect to the high sensitivity of XANES to small structural and electronic changes,[44] a very small decrease in the white line intensity was observed from D3-F to D1-F. The comparison with the Au foil suggested a partial dealloying in the samples by increasing the OlAc content, which is in-line with the XRD results. The same trend, which eventually became more visible, was observed in the XANES spectra at the Cu K-edge (Fig. S5b†). Indeed, D1-F showed a less intense pre-edge peak at an energy of 8980 eV than those of D2-F and D3-F. This decrease in the intensity (Fig. S5b†) suggested a decrease in the fraction of Cu alloyed with Au, which is in agreement with the increase in the volume of OlAc, which acted as the oxidizing agent in the synthesis. The XANES spectra of the fresh samples at the Fe K-edge were all representative of magnetite. This is evident by the comparison with the reference spectra. Furthermore, a decrease
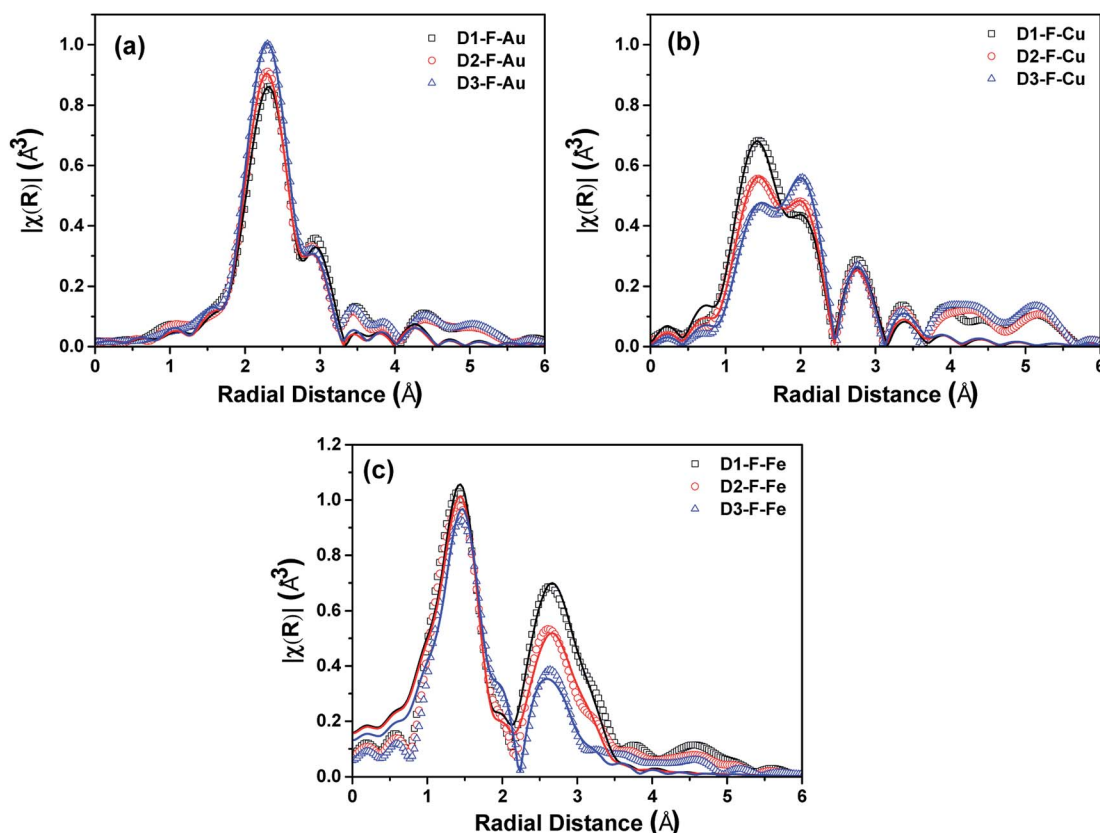

Fig. 4 The magnitude of the Fourier transforms of the $k^2\chi(k)$ for the fresh NCs at different edges of (a) Au-L$_3$, (b) Cu−K and (c) Fe−K. The scattered points are the experimental data while the solid lines represent the fitted profiles.
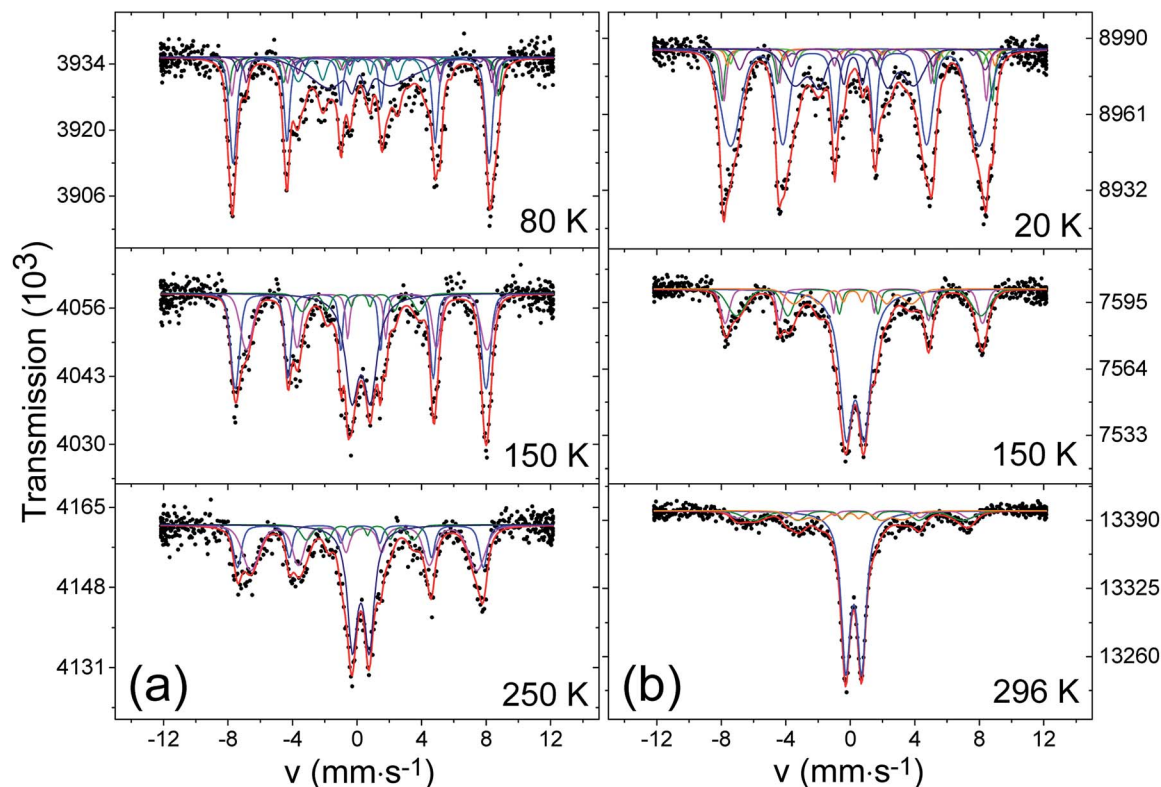
Fig. 5 Mössbauer absorption spectra taken at different temperature for samples D1-F (a) and D3-F (b).

in the intensity of the white lines is observed from D1-F to D3-F (Fig. S5c†). This decrease could be attributed to the lower crystallinity of the sample when the population of the NCs with a core/shell morphology in the MOx increased, as is also suggested by XRD. All samples also featured a pre-edge peak at an energy of ~7114 eV which could be attributed to the 1s to 3d transition, suggesting the existence of non-centrosymmetric absorption sites such as tetrahedral positions,[45,46] which exist in the magnetite crystalline structure.

The EXAFS functions were also analyzed (see Fig. S6†). The $k^2\chi(k)$ of the fresh NCs at the Au L_3-edge and the magnitude of their Fourier transforms (|FT|) are shown in Fig. S6a† and 4a, respectively. The $k^2\chi(k)$ and |FT| were quite similar, though a small shift was observed in the data of the k space, suggesting that there is a slightly different environment around the Au absorbers. This can be in line with the XRD results, from which we found that the AuCu phase was more preserved at the lowest level of OlAc $i.e.$ for D3-F. On the other hand, the first peak of the FT reduced from the D1-F to the D3-F. In agreement with this, the results of the fitting procedure demonstrated a decrease in the Au–Cu coordination number, though the error of the calculated CN should be taken into account while making an assessment (see Table S1†). The same applies to the CN of the Au–Au first shell, which is representative of the Au phase (see Table S1†). Nevertheless, the considerable contribution of the Au phase in the scattering, which was almost 50% in all cases, suggested the existence of clusters of Au or Au-rich phases that

were not detectable by XRD, resulting in a local deformation of the ordered alloy.

A similar trend for the partial dealloying of AuCu was also observed from the data at the Cu K-edge. As shown in Fig. S6b,† the oscillations slightly shifted to higher energies from D1-F to D3-F. This indicates that there are fewer scattering contributions from the atoms in the first shell in the vicinity of Cu absorbers at a low radial distance. Indeed, the |FT| revealed a peak at a low radial distance of 1.4 Å (see Fig. 4b) which is typically observed for oxygen-coordinated metal absorbers.[47–50] The presence of CuO could be discarded by the XANES results, particularly by the position of the edge feature of the spectra.[51,52] It is noteworthy that the simulations of the EXAFS signal were successful only considering the AuCu and Cu_2O phases, rather than CuO. The simulation of the EXAFS showed an increase in the CN of the Cu–Au shell in the AuCu phase from D1-F to D3-F, which was coupled with a decrease in the CN for the Cu–O shell in the Cu_2O phase (see Table S2†). Furthermore, in this case, the magnitude of the σ^2 factor for the Cu atoms suggests the disordered nature of the alloy in our samples, with a deviation from the model cluster of an ordered alloy.

The $k^2\chi(k)$ at the Fe K-edge (Fig. S6c†) showed a shift to higher energies from D1-F to D3-F, which suggests that there is a decrease in the oxidation extent of Fe in the samples. The |FT| of the samples at the Fe K-edge (Fig. 4c) showed a profile that is typical for a structure that has both octa and tetrahedral cation positions, which is consistent with the presence of the magnetite/maghemite phase. The CNs for the shells relating to

the Fe and O scatterers at the octahedral and tetrahedral absorbers both showed a decrease from D1-F to D3-F. However, considering the uncertainty in the estimation of these parameters, a clear trend cannot be ascertained (see Table S3†). Nevertheless, the σ^2 factor for the Fe increased from D1-F to D3-F, indicating a more inhomogeneous distribution of Fe in the NCs, which arises from the increasing contribution of the amorphous iron-containing phase. Only in the D3-F sample, a small contribution of ∼20% was observed in the EXAFS from the Fe–Fe shell, corresponding to a metallic Fe phase, which was not detected by other techniques but is still in line with the observed shift of the EXAFS in the k space.

3.2. Results from Mössbauer spectroscopy

We performed Mössbauer spectroscopy to learn more about the composition and magnetism as viewed by the hyperfine interactions at the ^{57}Fe local probe. Spectra from D1-F and D3-F were taken at various temperatures and are shown in Fig. 5a and b. As expected from the complex structure of the materials, the

hyperfine spectra are complicated by the presence of various local surroundings of Fe and from fits to the spectra one can only expect information on the major components.

At 250 K, the spectrum of D1-F reveals a superposition of several subspectra with a prominent non-magnetic quadrupole doublet (labeled A) in the center. In addition, a background of magnetic sextets can be seen. The asymmetric character of the absorption intensities with an apparent stronger absorption of the most positive absorption lines is an indicator for the presence of magnetite. In Table S4,† we give the hyperfine parameters that were used for the fit. The main contribution to this magnetic part of the spectrum consists of two spectra, attributed to octahedral and tetrahedral sites (M1 and M2), that have the expected center shifts and area ratios of about 2 : 1 as expected for magnetite. The magnetic hyperfine fields are slightly smaller than those of well-crystallized magnetite, and they show a distribution which is assumed to have a Gaussian profile that can be related to the irregular morphology of nano-sized domains. Also, timely fluctuating local magnetization may
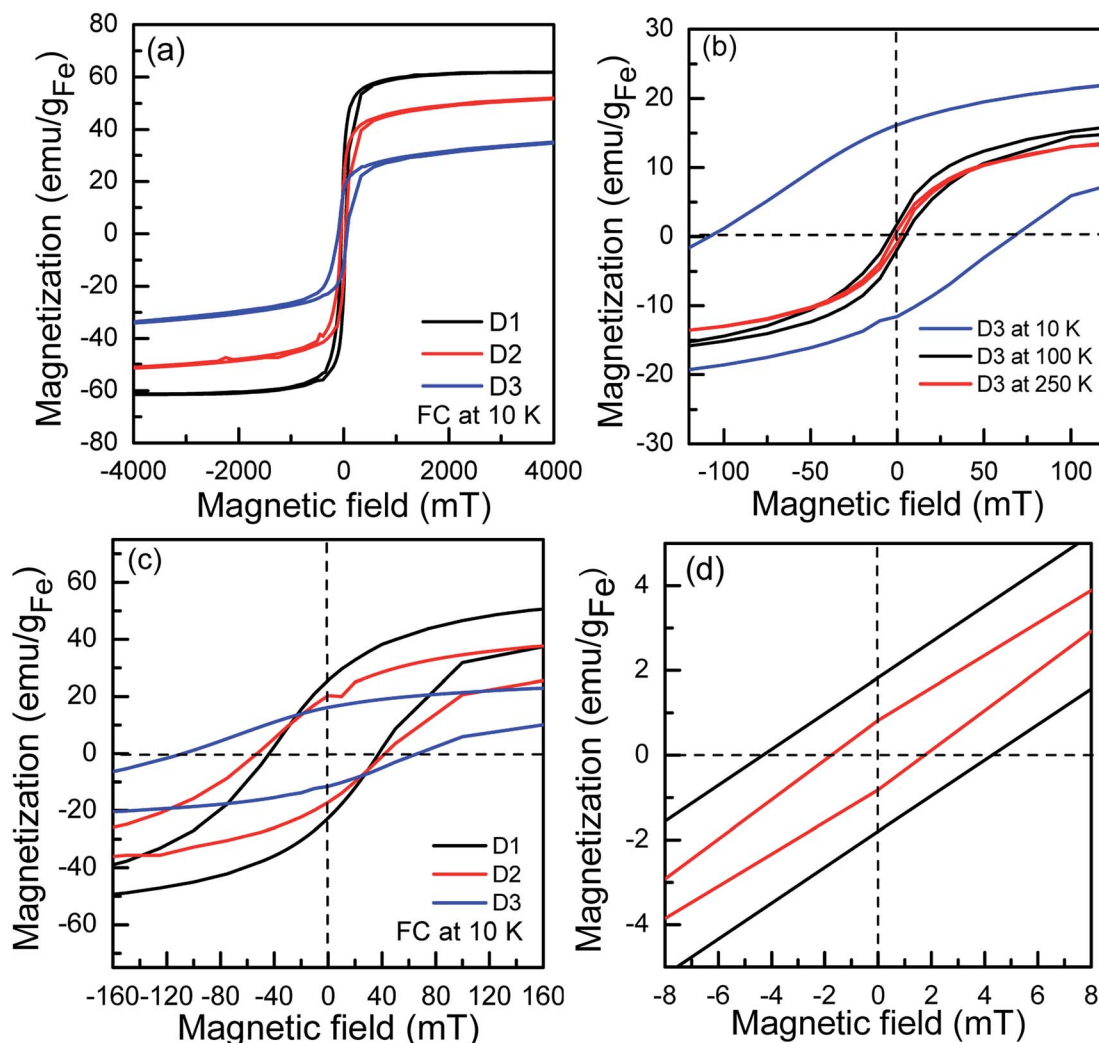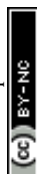

Fig. 6 (a) Field–cooled (FC) magnetization hysteresis loops of the samples measured at 10 K and (b) at different temperatures for D3-F. (c) and (d) show the magnified loops at small fields for (a) and (b), respectively.

play a role. These fluctuations are, however, not fast enough to lead to a superparamagnetic collapse of the magnetite pattern. This is in keeping with the relatively large size of magnetite domains that were seen in HRTEM. In addition to A, M1 and M2, we need a further strongly broadened magnetic pattern (M3) with a magnetic hyperfine field of 20 T and a center shift in the trivalent or even metallic range for the fit. The spectrum taken at 150 K can be fitted with the same strategy, yet at 80 K the doublet A has disappeared and the magnetic structures have become even more complex. One reason for this is that we are below the Verwey temperature of magnetite ($T_V \approx 120$ K), in which the two sites for Fe^{3+} in the tetrahedral (M2) sites and mixed-valent $Fe^{+2.5}$ in the octahedral (M1) sites are differentiated to at least 5 magnetically inequivalent sites. In nano-sized magnetite, even more sites have to be introduced.[53] Another reason is that, in our nano-compounds, one has to expect a wide distribution of Verwey transitions due to the locally inhomogeneous structure. For the fit attempt shown in Fig. 5, we introduced the hyperfine parameters derived in[53] for nano magnetites. The resonance area covered at higher temperatures under the doublet pattern is now contained in a sextet (AM, see Fig. 5a) with a magnetic hyperfine field of 49 T and a distribution with $\sigma \approx 0.6$. The hyperfine parameters of both the doublet at high temperature and the sextet developing at low temperature from it, suggest that they are due to an amorphous trivalent oxide close in composition to Fe_2O_3 as discussed, for example, in ref. 54. This is also in line with the poorly crystalline nature of the shell in our dumbbells-like NCs with core–shell MOx. The anomalously large linewidth 0.8 mm s^{-1} of the doublet and also the quadrupole splitting are supposed to be caused by a distribution of highly distorted oxygen coordination around the Fe^{3+}. A magnetic order of this kind of amorphous iron oxides typically occurs below 100 K, which is also consistent with our data. The fitting of the spectra of D3-F could be achieved in the same way. Notably, the contribution of magnetite decreased in comparison with D1-F (see Table S4†) at the expense of an increase in the amorphous oxide, which is consistent with the findings from XRD, XANES and EXAFS. Surprisingly, we were not able to resolve a signal of α-iron. We suppose that the reason for this is the very small size (only a few nanometers) which causes a superparamagnetic relaxation down to low temperatures, and the irregular shape of these particles having large surface fractions of iron that are bound to oxygen, resulting in a wide distribution of hyperfine parameters.

In both D1-F and D3-F, we could not trace a signature of FeO which above its magnetic transition around 200 K should show a doublet pattern with a center shift around 1.5 mm s^{-1}.[55]

The nature of the magnetic component M3, with a magnetic hyperfine field around 20 T and a relative resonance area of about 10% of the total iron for both D1-F and D3-F, remains unclear. Admittedly, it could be a fit artifact since, due to the inhomogeneous size of nano-sized domains of magnetite, there may be a distribution of fluctuation frequencies that was not taken into account. However, the hyperfine parameters are close to those reported for nano Fe–Cu alloys produced by ball-milling.[56]

### 3.3. Static magnetic properties

The maximum magnetization M_{max} shows a decreasing trend from sample D1-F to D3-F (Fig. 6). The observed trend indicates that there should be phase/structural differences between the three particles since they have identical iron oxide domain sizes. To gain deeper insight into magnetization, field-cooled (FC) hysteresis loops were recorded at 10 K in 5 T cooling magnetic fields (Fig. 6a and c). The FC loops reveal a shifted hysteresis loop towards negative field values. This phenomenon is the fingerprint of exchange bias H_{EB} interactions. The H_{EB} is estimated to be 20 mT for the D3-F which is comparable to the H_{EB} reported by Chandra et al. for Au–Fe$_3$O$_4$ dimers.[20] The H_{EB} is negligible for the D2-F, and it diminishes in the D1-F sample. The exchange bias (EB) interaction appears in magnetic systems that consist of two phases behaving differently in magnetic fields, one which is reversing opposite to the field (e.g. antiferromagnetic phase, FeO) and the other one does not (e.g. ferrimagnetic phase, Fe$_3$O$_4$). It has, however, been shown that H_{EB} can appear due to external strain,[57] disordered spins,[15] and interfacial stress at the interface of Au and Fe$_3$O$_4$ in heterostructured nanoparticles.[20] To clarify the origin of the EB in the studied system, FC loops of the D3-F sample were recorded at 100 and 250 K (see Fig. 6b and d). The fact that the H_{EB} disappears at 100 K rules out the presence of FeO as its magnetic transition temperature (the Néel temperature) is around 198 K, matching the Mössbauer spectroscopy results. Since there is a comparable Au–Fe$_3$O$_4$ interface volume in all the samples, the interfacial stress cannot account for the EB. As extracted from the Mössbauer spectroscopy, there is 65% amorphous (glass-like) γ-Fe$_2$O$_3$ in the D3-F sample and the magnetic transition is below 100 K. The glassy spins are frozen in an anisotropic configuration as the temperature drops below its transition temperature, behaving like a pinning layer, so they are presumably responsible for the appearance of the EB interaction. At 100 K, which is above its magnetic transition temperature, the spins become highly disordered and show no anisotropic configuration, thus causing no EB. The existence of EB as a result of super spin glass-like states has been demonstrated in hollow γ-Fe$_2$O$_3$.[15]

4. Summary and conclusions

To summarize, we have highlighted the significance of the OlAc in the synthesis of AuCu–Fe oxide dumbbell-like NCs and its effects on their final structural and magnetic properties (illustrated schematically in Scheme 2).

Using the highest amount of OlAc resulted in the formation of AuCu-magnetite dumbbell-like heterostructures. The presence of magnetite rather than maghemite was distinguished by XANES and Mössbauer as they provide the finger-print for the present phases. The magnetic properties were indeed consistent with those of magnetite NPs, due to the presence of a crystalline magnetite phase. The combination of XRD and XAFS analyses clearly evidenced a partial dealloying between the Au and Cu, which resulted in the formation of an inhomogeneous AuCu alloy coupled with the minor presence of a Cu$_2$O phase. This is in line with the oxidizing nature of the synthetic conditions in the presence of high amounts of OlAc.
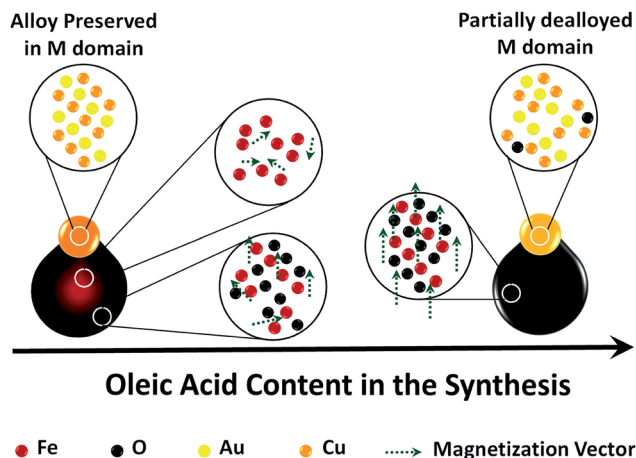
Scheme 2 Schematic summary of effect of changing the OlAc content in the synthesis.

Consistently, using the lowest amount of OlAc resulted in a better preservation of the AuCu alloy, as was evidenced by XAFS and XRD, but it considerably affected the magnetic properties. In this case, dumbbell-like NCs with a core–shell morphology in the MOx domain were formed. The core was richer in iron while the shell was more oxidized, consistent with the EFTEM results which showed a higher O density coupled with a lower Fe one in the MOx shell. Nevertheless, both the core and the shell in the MOx were poorly crystalline and highly disordered, as was evidenced by XRD and XAFS. Such a disorder caused a significant suppression of the magnetization. In this regard, Mössbauer results could indicate the presence of a glass-like maghemite phase which was likely distributed in the shell-region of the MOx. This highly disordered phase was also likely responsible for the observed exchange bias.

To conclude, the results herein reported highlight the importance of OlAc in defining the oxidation extent of Fe species, the crystallinity of the iron oxide domain and subsequently the magnetic properties of the synthesized nanocomposites. We claim that our results evidence a trade-off between obtaining a MOx domain with good magnetic properties and the preservation of alloys in the M domain in this type of heterostructures. If preserving the alloy in the M domain is desired, and such an alloy is sensitive to an oxidizing environment, one should keep the synthetic environment poorly oxidizing by reducing the amount of OlAc. This, in turn, has the drawback of obtaining poor magnetic properties. These findings can be potentially used as a guideline for the synthesis of similar nanocomposites to prevent a loss of desired properties.

Conflicts of interest

There are no conflicts to declare.

Acknowledgements

References

1 L. Wu, A. Mendoza-Garcia, Q. Li and S. Sun, Organic Phase Syntheses of Magnetic Nanoparticles and Their Applications, *Chem. Rev.*, 2016, **116**(18), 10473–10512.

2 H. Gu, X. Xu, H. Zhang, C. Liang, H. Lou, C. Ma, Y. Li, Z. Guo and J. Gu, Chitosan-coated-magnetite with Covalently Grafted Polystyrene Based Carbon Nanocomposites for Hexavalent Chromium Adsorption, *Engineered Science*, 2018, **1**, 46–54.

3 J. Huang, Y. Cao, Q. Shao, X. Peng and Z. Guo, Magnetic Nanocarbon Adsorbents with Enhanced Hexavalent Chromium Removal: Morphology Dependence of Fibrillar vs Particulate Structures, *Ind. Eng. Chem. Res.*, 2017, **56**(38), 10689–10701.

4 Y. He, S. Yang, H. Liu, Q. Shao, Q. Chen, C. Lu, Y. Jiang, C. Liu and Z. Guo, Reinforced carbon fiber laminates with oriented carbon nanotube epoxy nanocomposites: Magnetic field assisted alignment and cryogenic temperature mechanical properties, *J. Colloid Interface Sci.*, 2018, **517**, 40–51.

5 H. Wei, H. Gu, J. Guo, D. Cui, X. Yan, J. Liu, D. Cao, X. Wang, S. Wei and Z. Guo, Significantly enhanced energy density of magnetite/polypyrrole nanocomposite capacitors at high rates by low magnetic fields, *Advanced Composites and Hybrid Materials*, 2017, **1**(1), 127–134.

6 N. Wu, J. Qiao, J. Liu, W. Du, D. Xu and W. Liu, Strengthened electromagnetic absorption performance derived from synergistic effect of carbon nanotube hybrid with beads, *Advanced Composites and Hybrid Materials*, 2017, **1**(1), 149–159.

7 K. Gong, Q. Hu, L. Yao, M. Li, D. Sun, Q. Shao, B. Qiu and Z. Guo, Ultrasonic Pretreated Sludge Derived Stable Magnetic Active Carbon for Cr(VI) Removal from Wastewater, *ACS Sustainable Chem. Eng.*, 2018, **6**(6), 7283–7291.

8 W. Zijian, G. Sheng, C. Lei, J. Dawei, S. Qian, Z. Bing, Z. Zhaohui, W. Chen, Z. Min, M. Yingyi, Z. Xiaohong, W. Ling, Z. Mingyan and G. Zhanhu, Electrically Insulated Epoxy Nanocomposites Reinforced with Synergistic Core–Shell and Montmorillonite Bifillers, *Macromol. Chem. Phys.*, 2017, **218**(23), 1700357.

9 K. Gong, Q. Hu, Y. Xiao, X. Cheng, H. Liu, N. Wang, B. Qiu and Z. Guo, *J. Mater. Chem. A*, 2018.

10 S. Wei, Q. Wang, J. Zhu, L. Sun, H. Lin and Z. Guo, Multifunctional composite core-shell nanoparticles, *Nanoscale*, 2011, **3**(11), 4474–4502.

11 A. López-Ortega, M. Estrader, G. Salazar-Alvarez, A. G. Roca and J. Nogués, Applications of exchange coupled bi-magnetic hard/soft and soft/hard magnetic core/shell nanoparticles, *Phys. Rep.*, 2015, **553**, 1–32.

12 H. Khurshid, M.-H. Phan, P. Mukherjee and H. Srikanth, Tuning exchange bias in Fe/γ-Fe2O3 core-shell nanoparticles: Impacts of interface and surface spins, *Appl. Phys. Lett.*, 2014, **104**(7), 072407.

13 M.-H. Phan, J. Alonso, H. Khurshid, P. Lampen-Kelley, S. Chandra, K. Stojak Repa, Z. Nemati, R. Das, Ó. Iglesias and H. Srikanth, Exchange Bias Effects in Iron Oxide-Based Nanoparticle Systems, *Nanomaterials*, 2016, **6**(11), 221.

14 A. Lak, M. Kraken, F. Ludwig, A. Kornowski, D. Eberbeck, S. Sievers, F. J. Litterst, H. Weller and M. Schilling, Size dependent structural and magnetic properties of FeO-Fe3O4 nanoparticles, *Nanoscale*, 2013, **5**(24), 12286–12295.

15 Z. Nemati, H. Khurshid, J. Alonso, M. H. Phan, P. Mukherjee and H. Srikanth, From core/shell to hollow Fe/γ -Fe 2 O 3 nanoparticles: evolution of the magnetic behavior, *Nanotechnology*, 2015, **26**(40), 405705.

16 Z. Nemati, J. Alonso, H. Khurshid, M. H. Phan and H. Srikanth, Core/shell iron/iron oxide nanoparticles: are they promising for magnetic hyperthermia?, *RSC Adv.*, 2016, **6**(45), 38697–38702.

17 H. Khurshid, C. G. Hadjipanayis, H. Chen, W. Li, H. Mao, R. Machaidze, V. Tzitzios and G. C. Hadjipanayis, Core/shell structured iron/iron-oxide nanoparticles as excellent MRI contrast enhancement agents, *J. Magn. Magn. Mater.*, 2013, **331**, 17–20.

18 H. Khurshid, V. Tzitzios, W. Li, C. G. Hadjipanayis and G. C. Hadjipanayis, Size and composition control of core-shell structured iron/iron-oxide nanoparticles, *J. Appl. Phys.*, 2010, **107**(9), 09A333.

19 G. Zhang, Y. Liao and I. Baker, Surface engineering of core/shell iron/iron oxide nanoparticles from microemulsions for hyperthermia, *Mater. Sci. Eng. C*, 2010, **30**(1), 92–97.

20 S. Chandra, N. A. F. Huls, M. H. Phan, S. Srinath, M. A. Garcia, L. Youngmin, W. Chao, S. Shouheng, I. Òscar and H. Srikanth, Exchange bias effect in Au-Fe 3 O 4 nanocomposites, *Nanotechnology*, 2014, **25**(5), 055702.

21 C. Wang, C. Xu, H. Zeng and S. Sun, Recent Progress in Syntheses and Applications of Dumbbell-like Nanoparticles, *Adv. Mater.*, 2009, **21**(30), 3045–3052.

22 P. Guardia, S. Nitti, M. E. Materia, G. Pugliese, N. Yaacoub, J. M. Greneche, C. Lefevre, L. Manna and T. Pellegrino, Gold-iron oxide dimers for magnetic hyperthermia: the key role of chloride ions in the synthesis to boost the heating efficiency, *J. Mater. Chem. B*, 2017, **5**, 4587–4594.

23 S. Najafishirtari, P. Guardia, A. Scarpellini, M. Prato, S. Marras, L. Manna and M. Colombo, The effect of Au domain size on the CO oxidation catalytic activity of colloidal Au–FeOx dumbbell-like heterodimers, *J. Catal.*, 2016, **338**, 115–123.

24 S. Najafishirtari, T. M. Kokumai, S. Marras, P. Destro, M. Prato, A. Scarpellini, R. Brescia, A. Lak, T. Pellegrino, D. Zanchet, L. Manna and M. Colombo, Dumbbell-like Au0.5Cu0.5@Fe3O4 Nanocrystals: Synthesis, Characterization, and Catalytic Activity in CO Oxidation, *ACS Appl. Mater. Interfaces*, 2016, **8**(42), 28624–28632.

25 C. George, A. Genovese, A. Casu, M. Prato, M. Povia, L. Manna and T. Montanari, CO Oxidation on Colloidal Au0.80Pd0.20–FexOy Dumbbell Nanocrystals, *Nano Lett.*, 2013, **13**(2), 752–757.

26 S. Peng, C. Lei, Y. Ren, R. E. Cook and Y. Sun, Plasmonic/Magnetic Bifunctional Nanoparticles, *Angew. Chem., Int. Ed.*, 2011, **50**(14), 3158–3163.

27 H. Yu, M. Chen, P. M. Rice, S. X. Wang, R. L. White and S. Sun, Dumbbell-like Bifunctional Au–Fe3O4 Nanoparticles, *Nano Lett.*, 2005, **5**(2), 379–382.

28 C. Xu, B. Wang and S. Sun, Dumbbell-like Au-Fe3O4 nanoparticles for target-specific platin delivery, *J. Am. Chem. Soc.*, 2009, **131**(12), 4216–4217.

29 H. Kakwere, M. E. Materia, A. Curcio, M. Prato, A. Sathya, S. Nitti and T. Pellegrino, Dually responsive gold-iron oxide heterodimers: merging stimuli-responsive surface properties with intrinsic inorganic material features, *Nanoscale*, 2018, **10**(8), 3930–3944.

30 Y. Mao, P. Yi, Z. Deng and J. Ge, Fe3O4-Ag heterostructure nanocrystals with tunable Ag domains and magnetic properties, *CrystEngComm*, 2013, **15**(18), 3575–3581.

31 C. Xu, J. Xie, D. Ho, C. Wang, N. Kohler, E. G. Walsh, J. R. Morgan, Y. E. Chin and S. Sun, Au–Fe3O4 Dumbbell Nanoparticles as Dual-Functional Probes, *Angew. Chem., Int. Ed.*, 2008, **47**(1), 173–176.

32 Y. Zhai, L. Jin, P. Wang and S. Dong, Dual-functional Au-Fe3O4 dumbbell nanoparticles for sensitive and selective turn-on fluorescent detection of cyanide based on the inner filter effect, *Chem. Commun.*, 2011, **47**(29), 8268–8270.

33 F.-h. Lin and R.-a. Doong, Bifunctional Au–Fe3O4 Heterostructures for Magnetically Recyclable Catalysis of Nitrophenol Reduction, *J. Phys. Chem. C*, 2011, **115**(14), 6591–6598.

34 S. Najafishirtari, R. Brescia, P. Guardia, S. Marras, L. Manna and M. Colombo, Nanoscale Transformations of Alumina-Supported AuCu Ordered Phase Nanocrystals and Their Activity in CO Oxidation, *ACS Catal.*, 2015, **5**(4), 2154–2163.

35 C. Andrea Di, A. Giuliana, M. Marco, P. Emiliano, N. Nicola, C. Andrea and O. Luca, Novel XAFS capabilities at ELETTRA synchrotron light source, *J. Phys.: Conf. Ser.*, 2009, **190**(1), 012043.

36 G. Bunker, *Introduction to XAFS: A Practical Guide to X-ray Absorption Fine Structure Spectroscopy*, Cambridge University Press, Cambridge, 2010.

37 B. Ravel and M. Newville, ATHENA, ARTEMIS, HEPHAESTUS: data analysis for X-ray absorption spectroscopy using IFEFFIT, *J. Synchrotron Radiat.*, 2005, **12**(4), 537–541.

38 Z. Klencsár, *MossWinn*, 2016, http://www.mosswinn.com.

39 Z. Sun, L. Zhang, F. Dang, Y. Liu, Z. Fei, Q. Shao, H. Lin, J. Guo, L. Xiang, N. Yerra and Z. Guo, Experimental and simulation-based understanding of morphology controlled barium titanate nanoparticles under co-adsorption of surfactants, *CrystEngComm*, 2017, **19**(24), 3288–3298.

40 L. Zhang, W. Yu, C. Han, J. Guo, Q. Zhang, H. Xie, Q. Shao, Z. Sun and Z. Guo, Large Scaled Synthesis of Heterostructured Electrospun TiO2/SnO2 Nanofibers with an Enhanced Photocatalytic Activity, *J. Electrochem. Soc.*, 2017, **164**(9), H651–H656.

41 B. Song, T. Wang, H. Sun, Q. Shao, J. Zhao, K. Song, L. Hao, L. Wang and Z. Guo, Two-step hydrothermally synthesized

carbon nanodots/WO3 photocatalysts with enhanced photocatalytic performance, *Dalton Trans.*, 2017, **46**(45), 15769–15777.

42 D. Farrell, S. A. Majetich and J. P. Wilcoxon, Preparation and Characterization of Monodisperse Fe Nanoparticles, *J. Phys. Chem. B*, 2003, **107**(40), 11022–11030.

43 J. C. Bauer, D. Mullins, M. Li, Z. Wu, E. A. Payzant, S. H. Overbury and S. Dai, Synthesis of silica supported AuCu nanoparticle catalysts and the effects of pretreatment conditions for the CO oxidation reaction, *Phys. Chem. Chem. Phys.*, 2011, **13**(7), 2571–2581.

44 V. Krishnan, R. K. Selvan, C. O. Augustin, A. Gedanken and H. Bertagnolli, EXAFS and XANES Investigations of CuFe2O4 Nanoparticles and CuFe2O4–MO2 (M = Sn, Ce) Nanocomposites, *J. Phys. Chem. C*, 2007, **111**(45), 16724–16733.

45 Y. Yao, Y. Hu and R. W. J. Scott, Watching Iron Nanoparticles Rust: An *in situ* X-ray Absorption Spectroscopic Study, *J. Phys. Chem. C*, 2014, **118**(38), 22317–22324.

46 T. E. Westre, P. Kennepohl, J. G. DeWitt, B. Hedman, K. O. Hodgson and E. I. Solomon, A Multiplet Analysis of Fe K-Edge 1s → 3d Pre-Edge Features of Iron Complexes, *J. Am. Chem. Soc.*, 1997, **119**(27), 6297–6314.

47 N. K. Thanh, T. T. Loan, L. N. Anh, N. P. Duong, S. Soontaranon, N. Thammajak and T. D. Hien, Cation distribution in CuFe2O4 nanoparticles: Effects of Ni doping on magnetic properties, *J. Appl. Phys.*, 2016, **120**(14), 142115.

48 S. G. Kwon, S. Chattopadhyay, B. Koo, P. C. dos Santos Claro, T. Shibata, F. G. Requejo, L. J. Giovanetti, Y. Liu, C. Johnson, V. Prakapenka, B. Lee and E. V. Shevchenko, Oxidation Induced Doping of Nanoparticles Revealed by *in situ* X-ray Absorption Studies, *Nano Lett.*, 2016, **16**(6), 3738–3747.

49 H. Aritani, T. Tanaka, T. Funabiki, S. Yoshida, M. Kudo and S. Hasegawa, Structure of MoMg Binary Oxides in Oxidized/Reduced States Studied by X-ray Absorption Spectroscopy at the Mo K Edge and Mg K Edge, *J. Phys. Chem.*, 1996, **100**(13), 5440–5446.

50 A. A. Komlev, T. L. Makarova, E. Lahderanta, P. V. Semenikhin, A. I. Veinger, T. V. Tisnek, G. Magnani, G. Bertoni, D. Pontiroli and M. Ricco, Magnetism of aniline modified graphene-based materials, *J. Magn. Magn. Mater.*, 2016, **415**, 45–50.

51 H. Jin, R. You, S. Zhou, K. Ma, M. Meng, L. Zheng, J. Zhang and T. Hu, In-situ DRIFTS and XANES identification of copper species in the ternary composite oxide catalysts CuMnCeO during CO preferential oxidation, *Int. J. Hydrogen Energy*, 2015, **40**(10), 3919–3931.

52 P. Kappen, J.-D. Grunwaldt, B. S. Hammershøi, L. Tröger and B. S. Clausen, The State of Cu Promoter Atoms in High-Temperature Shift Catalysts—An *in situ* Fluorescence XAFS Study, *J. Catal.*, 2001, **198**(1), 56–65.

53 I. Dézsi, C. Fetzer, Á. Gombkötő, I. Szűcs, J. Gubicza and T. Ungár, Phase transition in nanomagnetite, *J. Appl. Phys.*, 2008, **103**(10), 104312.

54 L. Machala, R. Zboril and A. Gedanken, Amorphous Iron(III) OxideA Review, *J. Phys. Chem. B*, 2007, **111**(16), 4003–4018.

55 C. A. McCammon and D. C. Price, Mössbauer spectra of Fe x O (x>0.95), *Phys. Chem. Miner.*, 1985, **11**(6), 250–254.

56 F. M. Lucas, B. Trindade, B. F. O. Costa and G. Le Caër, Mechanical Alloying of Fe-Cu Alloys from As-Received and Premilled Elemental Powder Mixtures, *Key Eng. Mater.*, 2002, **230–232**, 631–634.

57 S. Kobayashi, S. Takahashi, Y. Kamada and H. Kikuchi, Strain-Induced Exchange Bias Effects in Chemically Ordered Pt3Fe Single Crystal, *IEEE Trans. Magn.*, 2008, **44**(11), 4225–4228.